This is the Author's Accepted Manuscript version

of the published article available at

https://doi.org/10.1016/j.ymssp.2022.109379

An adjustable device to adaptively realise diverse nonlinear force-displacement characteristics

Gianluca Gatti

Department of Mechanical, Energy and Management Engineering

University of Calabria

V. P. Bucci 46C, 87036, Rende (CS), Italy

e-mail: gianluca.gatti@unical.it

orcid: https://orcid.org/0000-0001-6390-8073

N° of Figures: 23

N° of Animations: 1

ABSTRACT

The benefit of introducing nonlinear stiffness elements to improve the dynamic performance of vibration energy harvesters, vibration isolators and vibration absorbers have attracted great attention in the recent literature. A simple adjustable device to tailor nonlinear stiffness for diverse engineering applications is thus proposed in this paper. The device adopts two pairs of linear oblique springs, whose geometric arrangement can be modified to achieve specific nonlinear force-displacement characteristics. Depending on its design configuration, it is able to be adapted and

behave as linear, hardening, softening, quasi-zero stiffness for large deflections, quasi-zero stiffness for small deflections, bi-stable and tri-stable. The design strategy and the main parameters involved are discussed.

KEYWORDS: Vibration energy harvester; vibration isolator; nonlinear energy sink; vibration absorber; quasi-zero stiffness; negative stiffness.

1 INTRODUCTION

Nonlinear stiffness, achieved by mechanical elements exhibiting a nonlinear force-displacement characteristic, has been extensively introduced on purpose into dynamical systems, to improve their performance, or make them lighter and compact [1]. Examples may be found in vibration energy harvesting [2,3], vibration isolation [4,5] vibration absorption [6,7], shock isolation [8]. Nonlinear force-displacement relationships have also been reported in nature and in biological systems. For example, the force–length relation of skeletal muscles [9], the elastic energy storage in hopping kangaroos [10], the jumps in humans [11], the prey capture mechanism in toads [12]. These have inspired pioneering engineering structures mimicking the fundamental behaviour, as for example discussed in [13,14,15].

Usually, nonlinear stiffness is achieved by the combination of positive and negative stiffness elements in parallel. The archetypal smooth and discontinuous oscillator with irrational nonlinearity [16-19] is an example of such combination, where the typical phenomenon is the dynamics transition from smooth to discontinuous depending on the smooth changing of a geometrical parameter.

Several application examples have been reported where nonlinear behaviour has been realised using different means, such as geometric arrangement of linear springs [20-24], combination of linkages and springs [25,26], X-shaped or scissor-like structures [27,28], magnets [29,30], buckling beams [31,32] and compliant structures [33,34].

Among the different types of nonlinear force-displacement curves, the following behaviours have been exploited for good use in engineering applications: quasi-zero stiffness, hardening or softening nonlinearity, softening-hardening stiffness, bi-stability and tri-stability.

Quasi-zero stiffness behaviour for small displacements has been used to design vibration isolators [13,35,36], and essentially nonlinear devices, such as energy sinks and vibration absorbers [30,37,38]. Predominantly hardening behaviour has been used to design energy harvesters [39], tuned mass dampers [40,41] and vibration neutralisers [42]. Predominantly softening behaviour has been used for energy harvesters [43] and mass dampers [40]. Softening-hardening behaviour, exhibiting quasi-zero stiffness (i.e. constant force) for large deflections, has been used in vibration isolators [44], to enlarge the elastic potential energy in catapults [45], or to realize soft gripping for robotic applications [46]. Bi-stable force-displacement characteristics [47] have been exploited for energy harvesting [48], micro-air vehicles [49], and also for vibration isolation [50]. The tri-stable force-displacement characteristic has been more recently exploited for energy harvesting, since it offers more probability for inter-well oscillations respect to bi-stable oscillators, even under low level excitation [2,20,51].

Nonetheless, classical linear springs are still an optimal mean in those cases where the source of vibration is predominately harmonic, as for example in harvesting energy from passing trains [52,53] or absorbing vibration at a troublesome resonance [54].

Usually, to meet required specifications, a design strategy is adopted to determine the system parameters, which then remain fixed during working conditions. Although some degree of tuning could be possible by adaptively modifying some of the system parameters (e.g. spring stiffness, magnets spacing, magnetic flux density), a large qualitative and quantitative change in the overall stiffness characteristic may not be practically attainable. Introducing additional mechanical elements into the system would increase the number of design parameters that can be changed in order to increase the degree of tuning, however this would involve making the device less robust and compact.

Customizing nonlinear stiffness would be attractive to better meet desired force-displacement characteristics, and recently, translating cam-like profiles have been proposed and investigated for such purposes [55]. Although this is a very smart strategy to tailor nonlinear stiffness at the design stage, it does not solve the issue of making the device adjustable during operation, as a specific cam profile cannot be easily changed during working conditions.

To overcome such limitation, this paper presents a study where a specific spring configuration is adopted, which is prone to be easily and adaptably changed during operation, according to the desired need. The proposed device is mechanically robust, since consisting of few mechanical components, extremely compact and thus reliable. It can be easily applied to vibration energy harvesting, vibration isolation, and vibration absorption, even in presence of large variations of working environment and operating conditions.

By acting on one single control parameter only, different qualitative and quantitative shapes of the force-displacement curve, and thus the stiffness, can be effectively realised: quasi-linear, hardening, softening, quasi-zero, softening-softening-hardening, softening-constant-hardening, softening-hardening-hardening, bi-stable and tri-stable characteristics can be achieved. Such property makes the proposed device suitable for different design purposes and applications, or even adaptable to different needs over time.

Following this introduction, Section 2 presents the fundamental unit of the system and its mathematical modelling, focusing on the different shapes of the force-displacement characteristics that can be obtained. Section 3 illustrates one of the simplest possible way to mechanically realise an adjustable oscillator, and Section 4 investigates the dynamic behaviour of the oscillator in the different configurations. Section 5 finally draws the conclusion of this work.

2 SYSTEM MODELING

The model of the oscillator proposed in this work is illustrated in Figure 1, in its static equilibrium configuration. It consists of a mass m, supported by a vertical linear spring of stiffness k_v. A set of

four symmetrical linear springs of stiffness *k*, arranged in an oblique configuration, are introduced to tailor the global force-deflection characteristic. An equivalent linear viscous damper *c* is introduced to model dissipative effects for dynamic purposes. The geometrical parameters that can be adjusted, thus modifying the stiffness characteristics, are *a* and *b*, which are labelled in Figure 1. The oscillator is supposed to be excited at its base by an imposed displacement *y*.

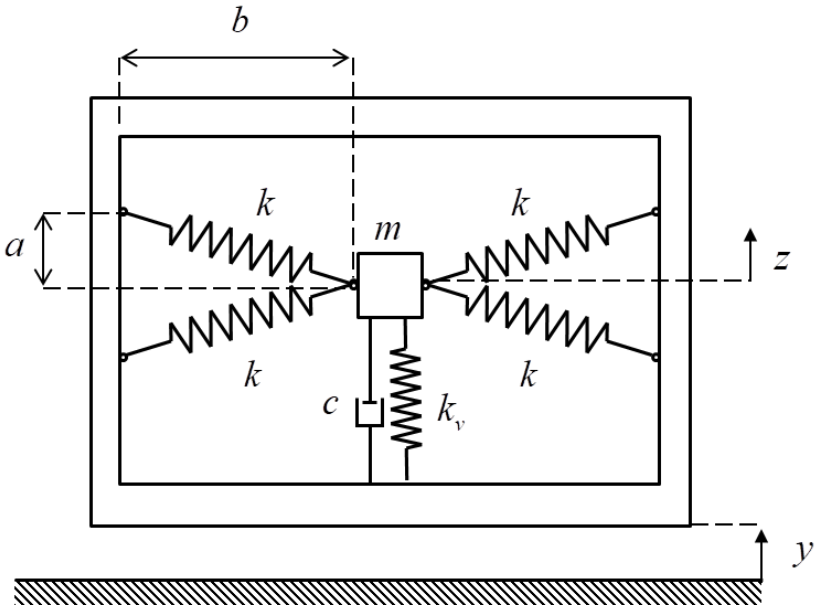


Figure 1. Model of the oscillator under study

The relation between the relative displacement z and the restoring static force *f* is given by

$$f = k_v z + 2k\left(-(a-z)\left(1-\frac{l_0}{\sqrt{b^2+(a-z)^2}}\right)+(a+z)\left(1-\frac{l_0}{\sqrt{b^2+(a+z)^2}}\right)\right) \tag{1}$$

where l_0 is the free length of the oblique springs.

It is then convenient to normalize Eq. (1) by the length l_0 and the vertical stiffness k_v, to yield

$$\hat{f} = \hat{z} + 2\hat{k}\left(-(\hat{a}-\hat{z})\left(1-\frac{1}{\sqrt{\hat{b}^2+(\hat{a}-\hat{z})^2}}\right)+(\hat{a}+\hat{z})\left(1-\frac{1}{\sqrt{\hat{b}^2+(\hat{a}+\hat{z})^2}}\right)\right) \tag{2}$$

where $\hat{f} = f/l_0k_v$ is the non-dimensional force, $\hat{z} = z/l_0$ is the non-dimensional displacement, and $\hat{k} = k/k_v, \hat{a} = a/l_0, \hat{b} = b/l_0$ are the fundamental non-dimensional key-parameters.

The nonlinear stiffness of the system can be obtained by taking the first derivative of Eq. (2) to yield

$$\frac{\partial \hat{f}}{\partial \hat{z}} = 1 + \hat{k}\left(4 + 2\hat{b}^2\left(-\frac{1}{\left(\hat{b}^2 + (\hat{a} - \hat{z})^2\right)^{3/2}} - \frac{1}{\left(\hat{b}^2 + (\hat{a} + \hat{z})^2\right)^{3/2}}\right)\right) \tag{3}$$

while the second derivative of Eq. (2) provides information about the curvature of the force-displacement curve, and it is given by

$$\frac{\partial^2 \hat{f}}{\partial \hat{z}^2} = 6\hat{b}^2\hat{k}\left(-\frac{(\hat{a} - \hat{z})}{\left(\hat{b}^2 + (\hat{a} - \hat{z})^2\right)^{5/2}} + \frac{(\hat{a} + \hat{z})}{\left(\hat{b}^2 + (\hat{a} + \hat{z})^2\right)^{5/2}}\right) \tag{4}$$

It can be seen that the limit of Eq.(3) for large displacement is given by

$$\hat{k}_0 = \lim_{\hat{z}\to\infty} \frac{\partial \hat{f}}{\partial \hat{z}} = 1 + 4\hat{k} \tag{5}$$

while Eq. (4) reduces to zero in the same limit, meaning that for very large displacement, the equivalent stiffness has a linear trend, with stiffness given by Eq. (5).

The stiffness at initial displacement, $\hat{z} = 0$, can be determined by a Taylor series approximation to give

$$\hat{k}_1 = 1 + 4\left(1 - \frac{\hat{b}^2}{\left(\hat{a}^2 + \hat{b}^2\right)^{3/2}}\right)\hat{k} \tag{6}$$

which can be solved to zero in terms of $\hat{a}$ to yield

$$\hat{a} = \hat{b}\sqrt{\frac{-1 + 2\hat{k}\left(-2 + \left(\frac{2 + 8\hat{k}}{\hat{b}^2\hat{k}}\right)^{1/3}\right)}{1 + 4\hat{k}}} \tag{7}$$

Equation (7) gives the relation among the non-dimensional key-parameters to achieve a Quasi-Zero-Stiffness (QZS) behaviour at small deflections, and thus provides the limiting condition between

positive and negative initial stiffness. In particular, when $\hat{k}_1 < 0$ then the system will be statically unstable at $\hat{z} = 0$. Equation (7) is plotted in Figure 2 as a solid line for $\hat{k} = 1$.

When the relative displacement increases, the nonlinear force-displacement curve will also be influenced by the higher terms in the Taylor series expansion. Due to the assumed symmetry of the force-displacement curve, the smaller non-zero term other than the first, given by Eq. (6), is the third and it is given below as

$$\hat{k}_3 = \frac{2\hat{b}^2\left(-4\hat{a}^2 + \hat{b}^2\right)\hat{k}}{\left(\hat{a}^2 + \hat{b}^2\right)^{7/2}} \tag{8}$$

For the force-displacement curve to exhibit a hardening behaviour it should then be $\hat{k}_1 > 0$ and $\hat{k}_3 > 0$. Thus equating Eq.(8) to zero gives the limiting condition as

$$\hat{a} = \frac{\hat{b}}{2} \tag{9}$$

which is linear and plotted in Figure 2 as a dotted line.

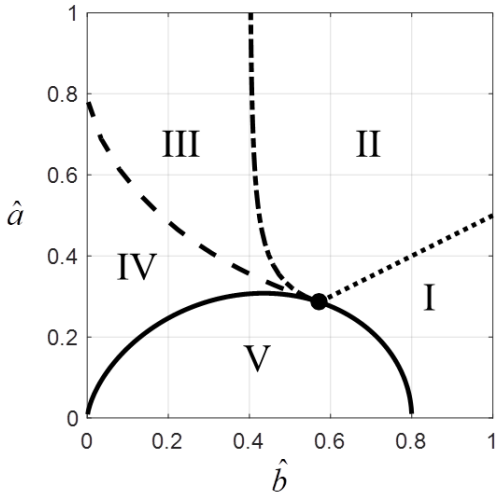


Figure 2. Different regions in the parameters plane achieving different behaviours in the force-displacement curve for $\hat{k} = 1$. I: hardening, II: softening-hardening-hardening, III: softening-softening-hardening, IV: tri-stable, V: bi-stable.

The spring arrangement in Figure 1, can also achieve a QZS for relatively large deflections, i.e. a softening-constant-hardening behaviour. The condition to realise such behaviour can be determined by simultaneously solving Eq. (3) and Eq. (4) set to zero. It was not possible to find a usable closed-form expression for such solution, so a numerical one was obtained. To better visualize such solution, this is pictorially illustrated in Figure 3(a) as the point of intersection (black dot) between the curves in Eq. (3) (solid lines) and in Eq. (4) (dash-dotted lines), for different values of the displacement where QZS is achieved, $\hat{z}_{\mathrm{QZS}}$. Such condition is plotted in Figure 2 as a dash-dotted line.

To find the limit for tri-stability, this is determined by simultaneously solving Eq. (2) and Eq. (3) set to zero, for different values of the displacement, $\hat{z}_{\mathrm{TRI}}$, which satisfies such conditions. Also in this case, it was not possible to find a usable closed-form expression, and a numerical solution was achieve, which is pictorially illustrated in Figure 3(b). Apart from the solutions indicated by the black dots in Figure 3, a trivial solution also exists for $\hat{b}=0$.

The limit for tri-stability is plotted in Figure 2 as a dashed line.

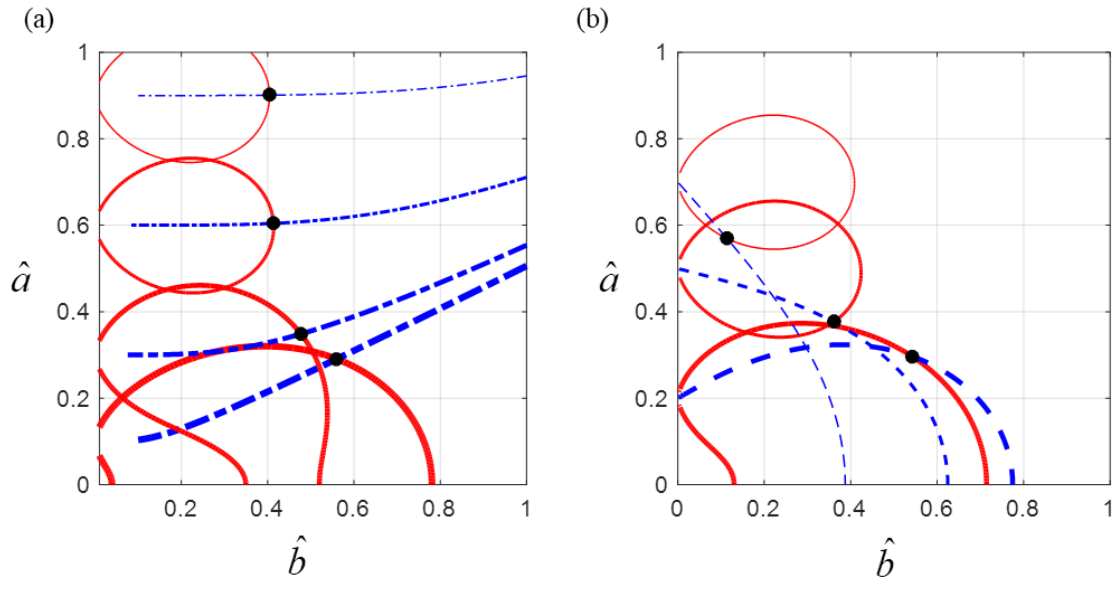


Figure 3. Pictorial representation of the condition for (a) softening-constant-hardening behaviour, and (b) tri-stabilty, in the parameters plane for $\hat{k}=1$. Solid lines correspond to Eq. (3), dash-dotted lines correspond to Eq. (4), dash lines correspond to Eq. (2), all set to zero. The black dots indicate the intersection points, and different line thickness denote different solutions: in (a) $\hat{z}_{\mathrm{QZS}}=0.1,\ 0.3,\ 0.6,\ 0.9$ from thicker to thinner; in (b) $\hat{z}_{\mathrm{TRI}}=0.2,\ 0.5,\ 0.7$ from thicker to thinner.

It can be then seen that all curves in Figure 2 intersect at a point C. The coordinates of this point in the parameters plane can be determined by substituting Eq. (9) into Eq. (7) set to zero, to yield

$$\mathrm{C}=\left\{\hat{b}_{\mathrm{C}},\hat{a}_{\mathrm{C}}\right\}=\left\{\frac{32\hat{k}}{\sqrt{5}(5+20\hat{k})},\frac{16\hat{k}}{\sqrt{5}(5+20\hat{k})}\right\} \tag{10}$$

Point C is indicated in Figure 2 by a black circle.

It can be noted that point C is a function of the non-dimensional stiffness only, and for very large values reaches the limit given below as

$$\lim_{\hat{k}\to\infty}\ \mathrm{C}=\left\{\frac{8}{5\sqrt{5}},\frac{4}{5\sqrt{5}}\right\}\approx\left\{0.715,0.358\right\} \tag{11}$$

How the coordinates of point C vary with the non-dimensional stiffness are illustrated in Figure 4.

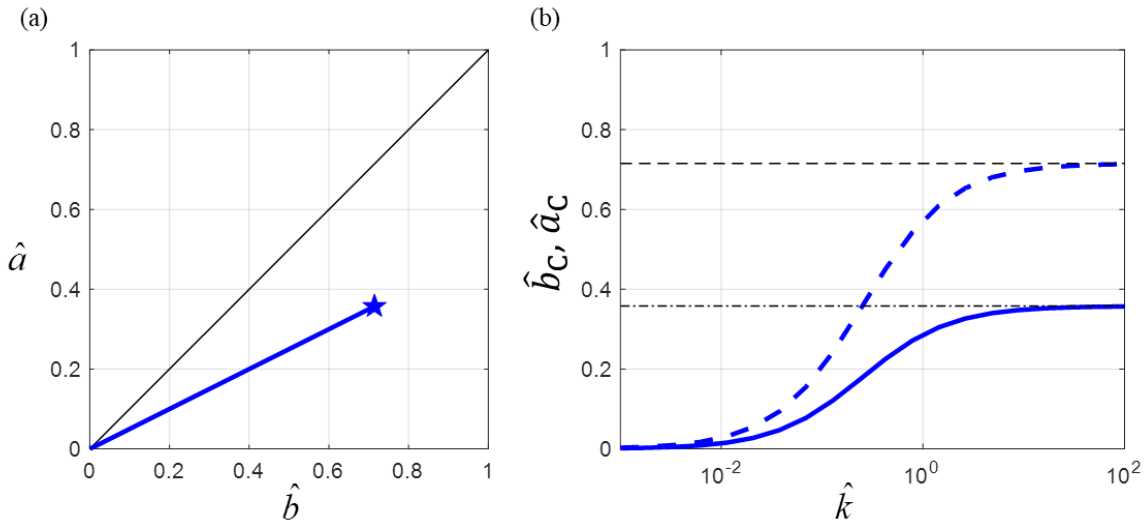


Figure 4. Coordinates of point C: (a) in the parameters plane and (b) as function of $\hat{k}$. In (a) the thin solid line identifies the diagonal for reference, the thick solid line identifies the trajectory of point C as the non-dimensional stiffness increases, and the star identifies the limit in Eq.(11). In (b) thick solid (dashed) line indicates the horizontal (vertical) coordinates of point C, the thin dash-dotted (dashed) line indicates the asymptotic trend of Eq. (11).

To visualize the shape of the force-displacement curves on the four boundaries depicted in Figure 2, they are illustrated in Figures 5(a-d), for different combinations of the geometric parameters and for $\hat{k}=1$. In particular, Figure 5(a) shows the case where geometric parameters are chosen along the solid line in Figure 2, Figure 5(b) shows the case where they are chosen along the dotted line in Figure 2, Figure 5(c) shows the case where they are chosen along the dash-dotted line in Figure 2, and Figure 5(d) shows the case where they are chosen along the dashed line in Figure 2. In all figures, the thin dashed line denotes the limit given by Eq. (5).

Figure 5(a) shows that when $\hat{b}$ is relatively small, the QZS behaviour for small deflection is followed by a region with negative stiffness. A hardening behaviour then manifests for higher values of $\hat{b}$. Figure 5(b) shows that, within the considered range of displacements, the hardening effect decreases as $\hat{b}$ increases, eventually leading to a quasi-linear behaviour. Figure 5(c) shows the QZS behaviour at relatively large deflections when the corresponding displacement, $\hat{z}_{\mathrm{QZS}}$, is increased. Figure 5(d) shows the limiting condition for a tri-stable behaviour, when the displacement at which this condition is achieved, $\hat{z}_{\mathrm{TRI}}$, is increased.

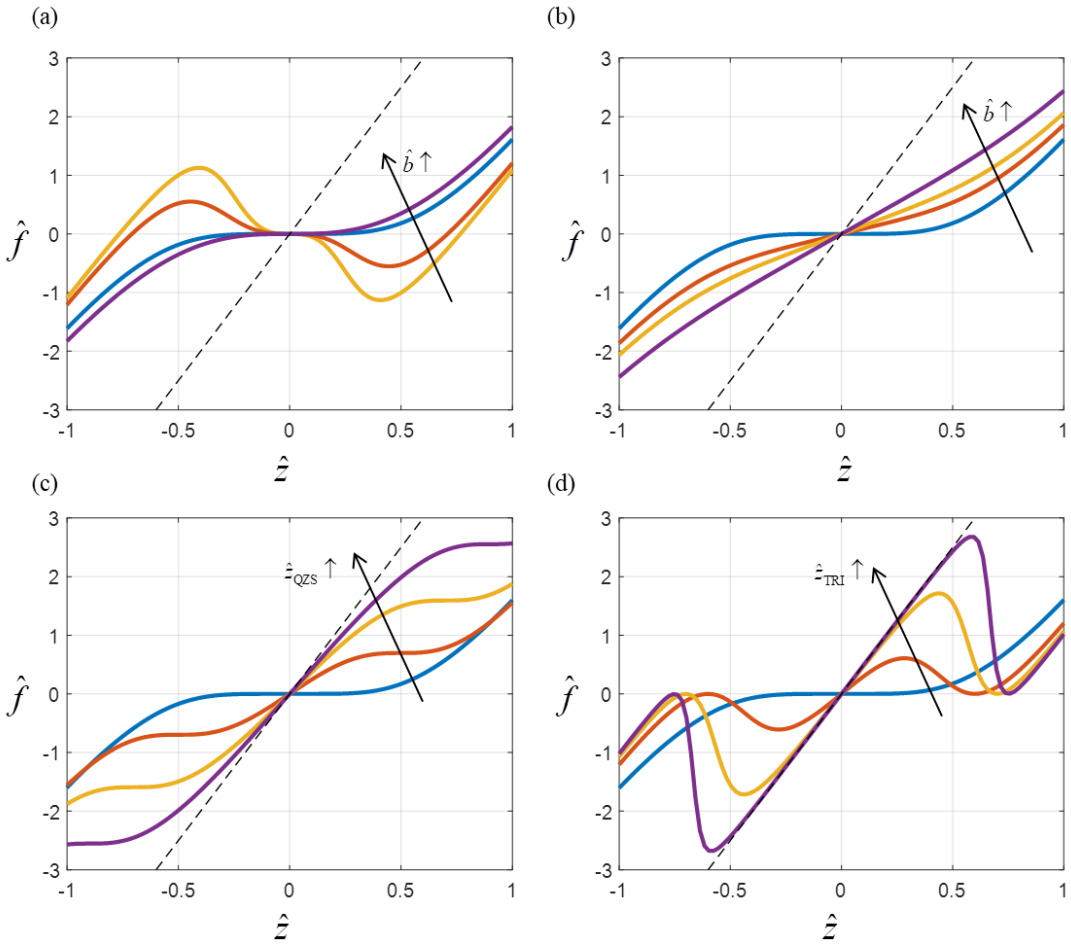


Figure 5. Force-displacement curves for different combinations of the geometric parameters and $\hat{k}=1$. (a) $\hat{b}=0.2, 0.3, \hat{b}_C, 0.75$, (b) $\hat{b}=\hat{b}_C,\ 0.7, 0.8, 1.0$, (c) $\hat{z}_{QZS}=0.09, 0.5, 0.7, 0.9$, (d) $\hat{z}_{TRI}=0.09, 0.6, 0.7, 0.75$. The thin dashed line denotes the limit given by Eq. (5).

To validate the analytical findings reported above, numerical simulations are performed for different values of the non-dimensional stiffness, $\hat{k}$, and different combinations of the non-dimensional geometric parameters, $\hat{a}$ and $\hat{b}$. The exact force-displacement relation in Eq.(2) and its first and second derivative in Eq.(3) and Eq.(4), respectively, are then numerically examined and each different characteristic is reported in Figure 6 using different markers. Also, a region of quasi-linear behaviour is numerically identified (and marked with small dots), where the stiffness has a relative deviation of less than 10%.

It can be seen that the closed-form expressions derived above and plotted in Figure 2, characterize the fundamental behaviour of the suspension stiffness and match the numerical investigation.

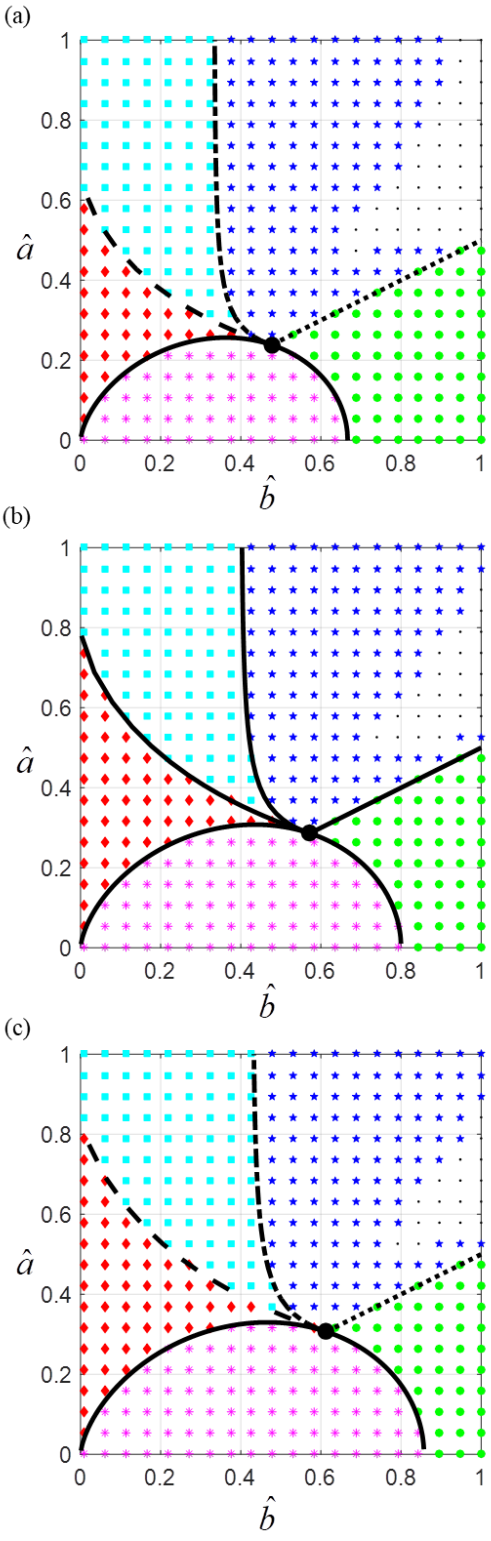


Figure 6. Numerical solutions of the force-displacement curves in the parameters plane for (a) $\hat{k} = 0.5$, (b) $\hat{k} = 1$ (c) $\hat{k} = 1.5$. Hardening behaviour (circles), softening-hardening-hardening behaviour (stars), softening-softening-hardening behaviour (squares), tri-stable behaviour (diamonds), bi-stable behaviour (asterisks), quasi-linear behaviour (dots).

3 MECHANICAL IMPLEMENTATION

Different mechanisms may be synthesised and incorporated into an adjustable device able to actively or adaptively modify the geometry of the oscillator, and thus changing its stiffness characteristic according to the needs. Among all the possible designs, perhaps, one of the simplest and most compact is illustrated in Figure 7. In particular, Figure 7(a) illustrates a computer aided design (CAD) model of the system, and Figure 7(b) overlaps the wireframe of the CAD model to the parameter regions identified in Section 2 and illustrated in Figure 6(b). The symmetric and synchronised adaptation of the parameters is achieved by using pairs of meshing gears, which are then driven by the single rotation of one of them, i.e. the control parameter θ. The outer spring attachments are located at a normalized parametric distance $\hat{c}$, which is labelled in Figure 7(b) along with control parameter θ. The specific configuration illustrated in Figure 7 shows the case where the non-dimensional distance among the wheel centres is 1 and the normalized distance $\hat{c}$ is 0.25. Such values are arbitrarily selected to illustrate the case where all the six regions are achievable with the adjustment of the control parameter.

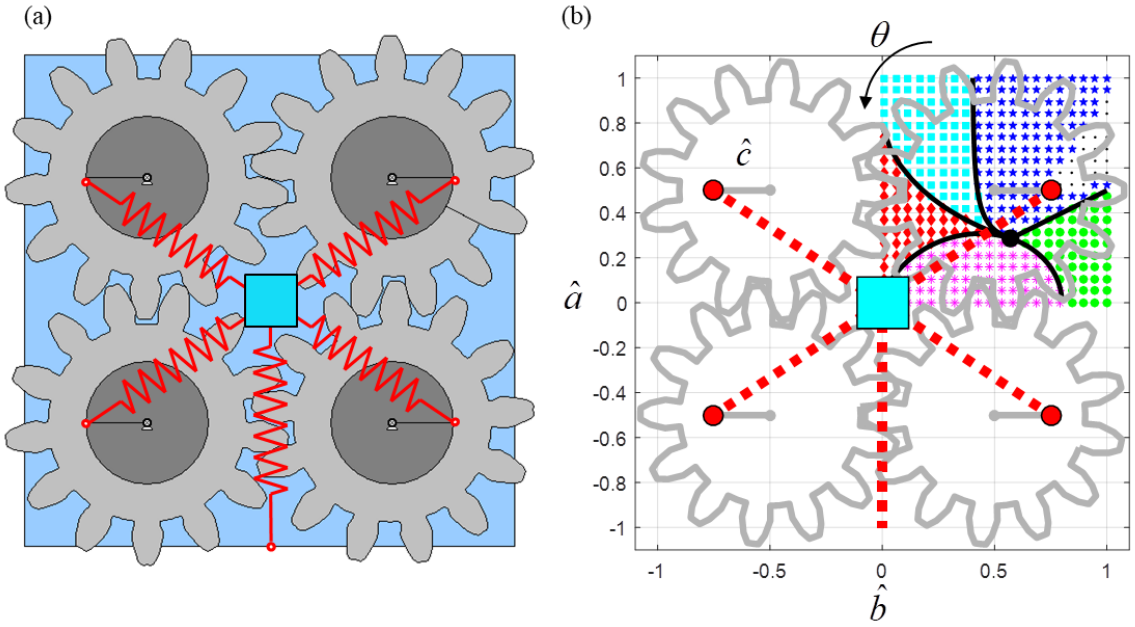


Figure 7. Mechanical implementation of the adjustable device: (a) CAD model, (b) wireframe model overlapped to the regions in the non-dimensional parameters plane.

Although different dimensioning may be achieved or optimized for the specific need, Figure 7(b) clearly shows how all the six regions may be achieved by a simple rotation of one wheel only. To better illustrates such a case, Figure 8 shows a tri-dimensional plot where the force-displacement curve in the $\hat{z} - \hat{f}$ plane varies with the angle of rotation θ, which is assumed to be zero in the configuration illustrated in Figure 7(b), and it is measured anti-clockwise on the upper-right wheel. In particular, Figure 9 to Figure 15 illustrate seven different configurations of the specific mechanism in Figure 7, and the corresponding force-displacement curves that can be achieved. The thin dashed lines in (b) denote the asymptotic trend, and the dots indicate the stable equilibrium points. An animation is also reported as a supplementary material in Appendix A.

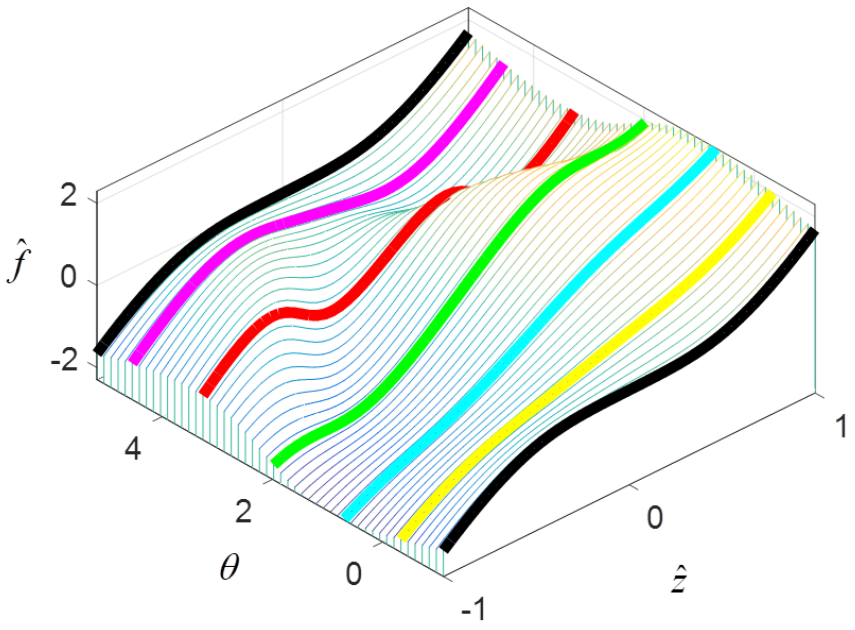


Figure 8. Force-displacement curve as a function of the rotation of one wheel from 0 to 2π.

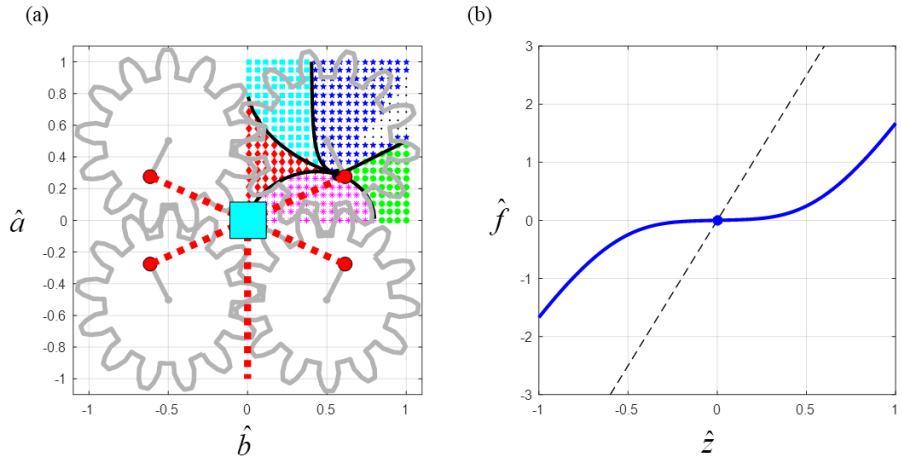


Figure 9. (a) Mechanism configuration and (b) force-displacement curve for $\theta = -1.1$.

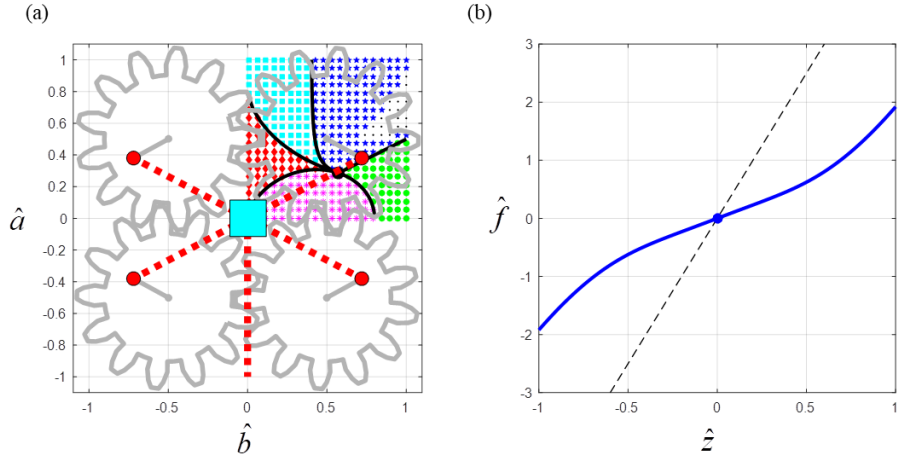


Figure 10. (a) Mechanism configuration and (b) force-displacement curve for $\theta = -0.5$.

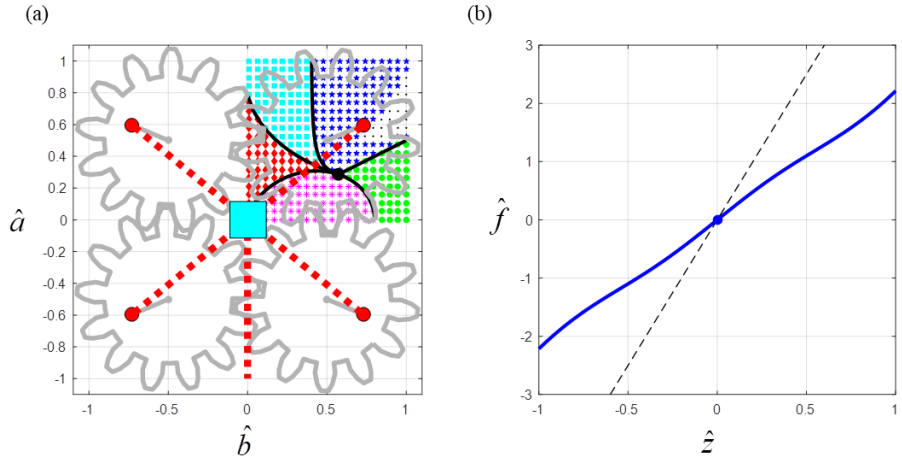


Figure 11. (a) Mechanism configuration and (b) force-displacement curve for $\theta = 0.4$.

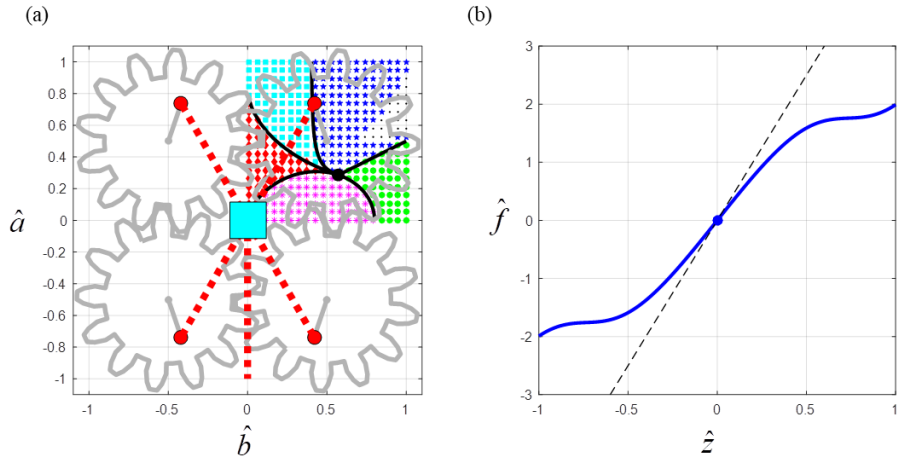


Figure 12. (a) Mechanism configuration and (b) force-displacement curve for $\theta = 1.9$.

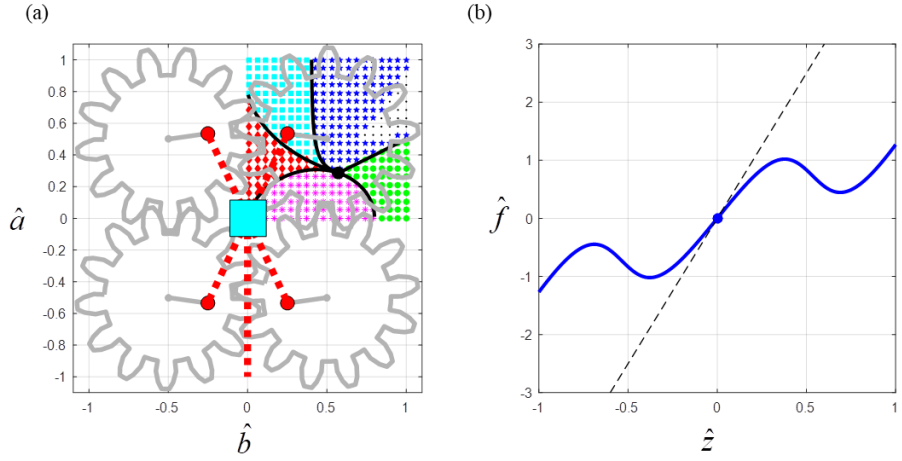


Figure 13. (a) Mechanism configuration and (b) force-displacement curve for $\theta = 3.0$.

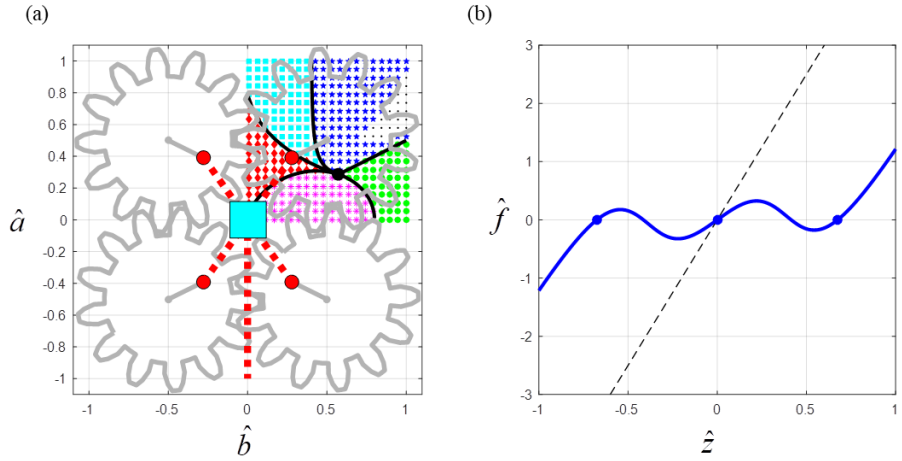


Figure 14. (a) Mechanism configuration and (b) force-displacement curve for $\theta = 3.6$.

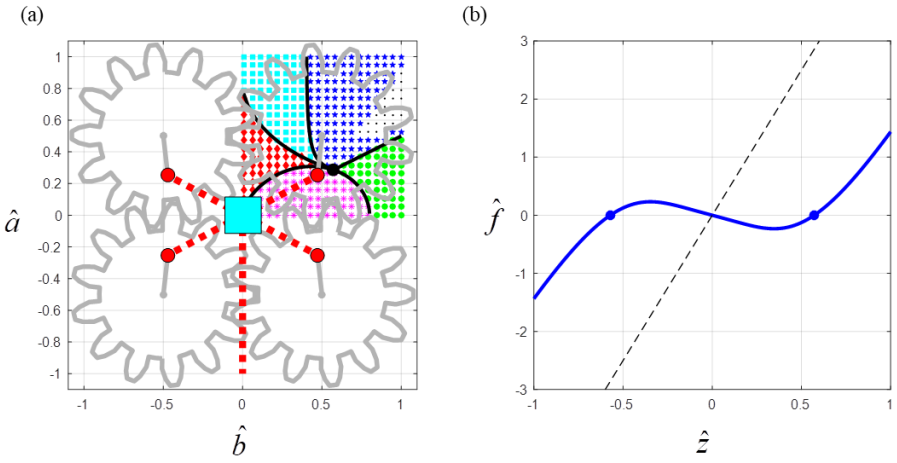


Figure 15. (a) Mechanism configuration and (b) force-displacement curve for $\theta = 4.6$.

4 DYNAMIC SIMULATIONS

In this section, the proposed system dynamics is analysed in term of the frequency response curve. To this end, the equation of motion of the oscillator in Figure 1 is reported below as

$$m\ddot{z} + c\dot{z} + f = -m\ddot{y} \tag{12}$$

where f is given by Eq. (1) and overdots indicates derivation respect to time t. Equation (12) can be conveniently rewritten in the following non-dimensional form, by assuming $y = Y\cos[\omega t]$,

$$\hat{z}'' + 2\zeta\hat{z}' + \frac{\hat{f}}{\hat{k}_0} = \hat{A}\cos[\Omega\tau] \tag{13}$$

where primes denote derivation respect to the non-dimensional time $\tau = \omega_0 t$, in which $\omega_0 = \sqrt{\hat{k}_0 k_v / m}$ and $\hat{k}_0$ is given in Eq. (5), $\zeta = c/2m\omega_0$ is the damping ratio, $\hat{f}$ is given by Eq. (3), $\Omega = \omega/\omega_0$ is the non-dimensional frequency, and $\hat{A} = \Omega^2\hat{Y}$ is the non-dimensional amplitude of the base acceleration, in which $\hat{Y} = Y/l_0$. Considering a constant amplitude acceleration is a practical assumption particularly when dealing with vibration energy harvesting [20] .

In order to find usable approximate closed-form expressions for the frequency response curve, the non-dimensional force $\hat{f}$ in Eq. (3) is approximated by a polynomial relation.

Although different studies have used classical Taylor series expansion around the static equilibrium configuration for relative small displacements, in the case reported in this paper, it was found that such an approximation was not enough and reliable to capture all the different stiffness characteristics for the whole range of geometrical parameters variation, in particular for large displacement values, i.e. up to $\hat{z}=1$. An odd 13-th order polynomial function of the displacement proved to capture the exact force-displacement curves satisfactorily. The need to go up to the 13-th term was motivated by the fact that seven boundary conditions were used, i.e. (i) the stiffness at zero displacement is set equal to that given by Eq.(6), the force, its first and second derivative are set equal to the corresponding exact one at (ii-iv) full-span ($\hat{z}=1$) and (v-vii) half-span ($\hat{z}=0.5$), respectively.

Equation (3) is then approximated by

$$\hat{f} \approx k_1\hat{z} + k_3\hat{z}^3 + k_5\hat{z}^5 + k_7\hat{z}^7 + k_9\hat{z}^9 + k_{11}\hat{z}^{11} + k_{13}\hat{z}^{13} \tag{14}$$

where the polynomial coefficients are reported in Appendix B.

By assuming a solution to the equation of motion, which is symmetric and predominately harmonic as $\hat{z} = \hat{Z}\cos[\Omega\tau + \varphi]$ where φ is the phase shift between the excitation and the response, applying the harmonic balance method, results in

$$-\Omega^2\hat{Z} + \hat{Z}G = \hat{A}\cos[\varphi] \tag{15}$$

$$2\zeta\hat{Z}\Omega = \hat{A}\sin[\varphi] \tag{16}$$

Squaring and adding Eqs. (15) and (16) gives the following relation between the displacement amplitude and frequency

$$\Omega^4\hat{Z}^2 + 2\Omega^2\hat{Z}^2\left(2\zeta^2 - G\right) + \left(\hat{Z}^2G^2 - \hat{A}^2\right) = 0 \tag{17}$$

where

$$G = k_1 + \frac{3}{4}k_3\hat{Z}^2 + \frac{5}{8}k_5\hat{Z}^4 + \frac{35}{64}k_7\hat{Z}^6 + \frac{63}{128}k_9\hat{Z}^8 + \frac{231}{512}k_{11}\hat{Z}^{10} + \frac{429}{1024}k_{13}\hat{Z}^{12} \tag{18}$$

It is noted that the amplitude-frequency equation in Eq.(17) is quadratic in Ω^2, and can be thus conveniently solved, to determine Ω as a function of Z. The steady-state dynamic response in terms of the frequency response curve follows a backbone, i.e. the unforced and undamped response, which is given by Eq. (15) as $\Omega_{backbone} = \sqrt{G}$

To limit the dynamic response at resonance, it is interesting to determine the relation among the damping ratio, the base excitation and the displacement response amplitude. This can be obtained from Eq.(16), when $\varphi = \pi/2$, and using the expression for the backbone curve, to give

$$\zeta = \frac{\hat{A}}{2\sqrt{G}\hat{Z}} \tag{19}$$

To limit the oscillator response within the range of the displacements used to plot the static curves in Sections 2 and 3, the amplitude response at resonance is set to 1, which gives $\zeta^* = \hat{A} \Big/ \left(2\sqrt{k_1 + 3/4k_3 + 5/8k_5 + 35/64k_7 + 63/128k_9 + 231/512k_{11} + 429/1024k_{13}}\right)$.

Figure 16(a) shows a tri-dimensional plot where the frequency response curves in the $\Omega - \hat{Z}$ plane varies with the angle of rotation θ. Figure 16(b) shows the view on the $\theta - \hat{Z}$ plane. In both figures, the grey contour indicates that the frequency response curve crosses the axis at $\Omega = 0$.

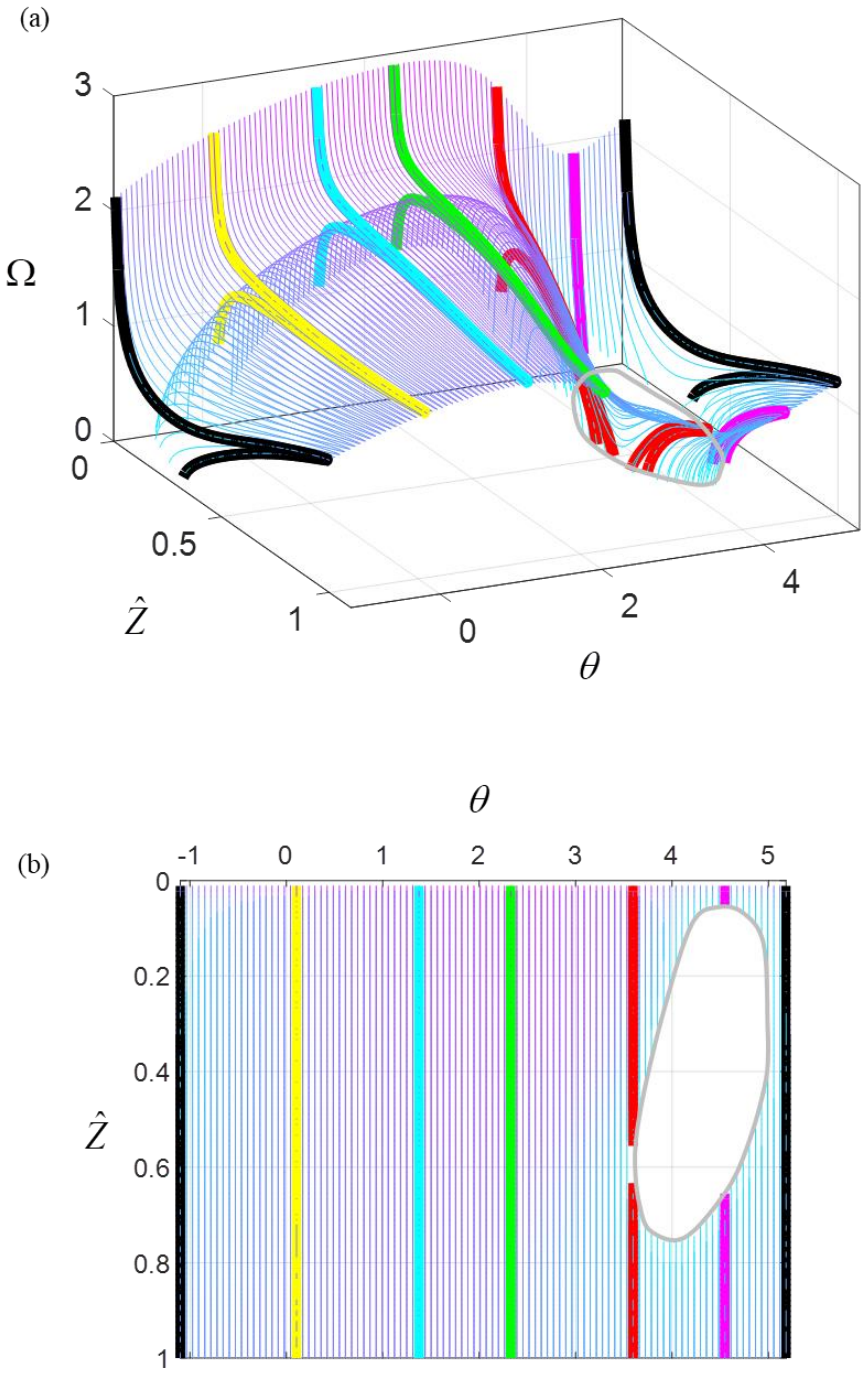


Figure 16. Frequency response curve as a function of the rotation θ of one wheel. (a) 3D view, (b) view on the $\theta - \hat{Z}$ plane.

The details of the frequency response curves, corresponding to the parameters of the actual mechanism, are presented in Figure 17 to Figure 23. In particular, parts (a) show the force-

displacement curve of the exact solution (solid line), the 13-th order polynomial approximation (thick dashed line) and 13-th order Taylor series approximation (thin dashed line). Parts (b) show the corresponding frequency response curve, where the response to a slow sweep-up and sweep-down are superimposed for validation. The backbone curve (thin dashed line) and the static equilibrium configurations (thin dash-dotted lines) are also indicated.

It can be clearly seen that a 13-th order Taylor series expansion fails to approximate the exact curve for large displacements. For completeness, the coefficients of the Taylor series expansion are reported in Appendix C. On the other hand, the polynomial expression in Eq. (14) captures relatively well all the different shapes of the force-displacement curves. The dynamic numerical simulations, performed using the exact force-displacement curve for the slow sweeps, show that the approximate frequency response curve are well captured, as well as the jump-up and jump-down frequencies.

For the case with tri-stable characteristic shown in Figure 22, an evident cross-well motion manifests up to the jump-down frequency, i.e. around $\Omega = 0.4$, both in the sweep-up and sweep-down. For about $\Omega > 0.5$, oscillation occurs around the stable static equilibrium solution at $\hat{Z} = 0$.

For the bi-stable characteristic shown in Figure 23, the assumed symmetric solution follows the frequency response curve up to the jump-down frequency again, at about 0.4. An evident cross-well motion manifests up to about 0.6. For higher frequencies, the oscillation evolves towards one of the two stable static equilibrium solutions, indicated by the upper and lower horizontal dash-dotted lines..

Since the aim of this paper is to show how the achieve different force-displacement curves with one mechanical device only, it is out of the scope of this study to investigate in further detail the dynamics of bi-stable and tri-stable oscillators, and the interested reader is directed to [2] for an insight.

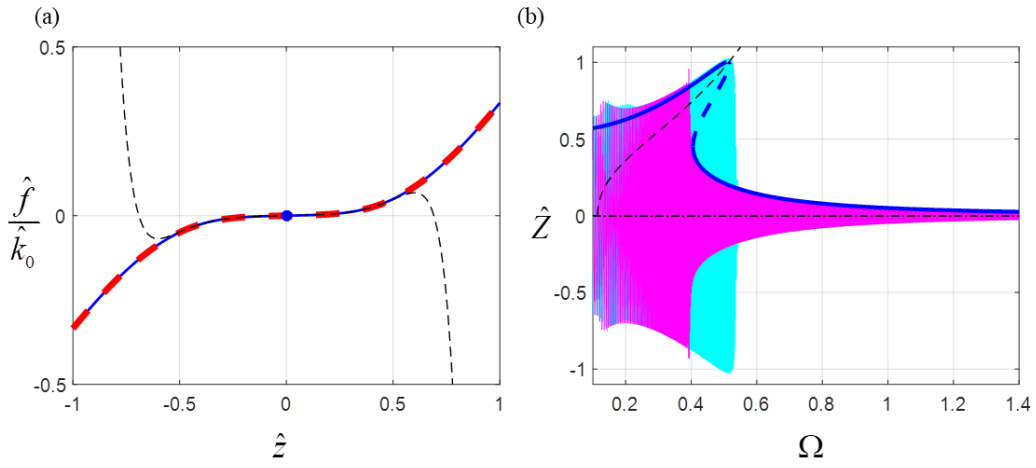


Figure 17. System response for $\theta = -1.1$. (a) Normalized force-displacement curve of exact (thick solid line), actual polynomial (thick dashed line) and Taylor polynomial (thin dashed line) solution. Small circles denote static equilibrium configurations. (b) Frequency response curve with stable (thick solid lines) and unstable (thick dashed lines) branches, backbone curve (thin dashed line), static equilibrium configuration (thin dash-dotted line, sweep-up (thin lighter/cyan line), and sweep-down (thin darker/magenta line).

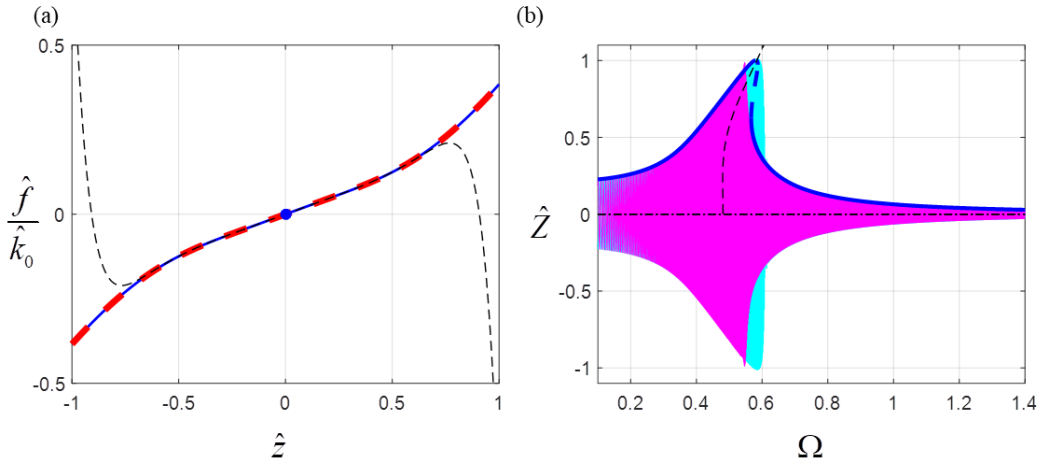


Figure 18. System response for $\theta = -0.5$. (a) Normalized force-displacement curve of exact (thick solid line), actual polynomial (thick dashed line) and Taylor polynomial (thin dashed line) solution. Small circles denote static equilibrium configurations. (b) Frequency response curve with stable (thick solid lines) and unstable (thick dashed lines) branches, backbone curve (thin dashed line), static equilibrium configuration (thin dash-dotted line, sweep-up (thin lighter/cyan line), and sweep-down (thin darker/magenta line).

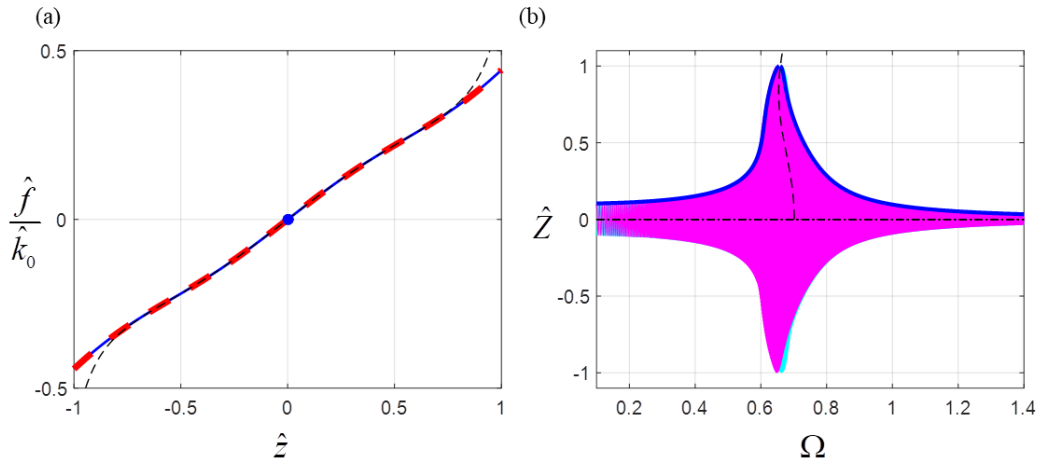


Figure 19. System response for $\theta = 0.4$. (a) Normalized force-displacement curve of exact (thick solid line), actual polynomial (thick dashed line) and Taylor polynomial (thin dashed line) solution. Small circles denote static equilibrium configurations. (b) Frequency response curve with stable (thick solid lines) and unstable (thick dashed lines) branches, backbone curve (thin dashed line), static equilibrium configuration (thin dash-dotted line, sweep-up (thin lighter/cyan line), and sweep-down (thin darker/magenta line).

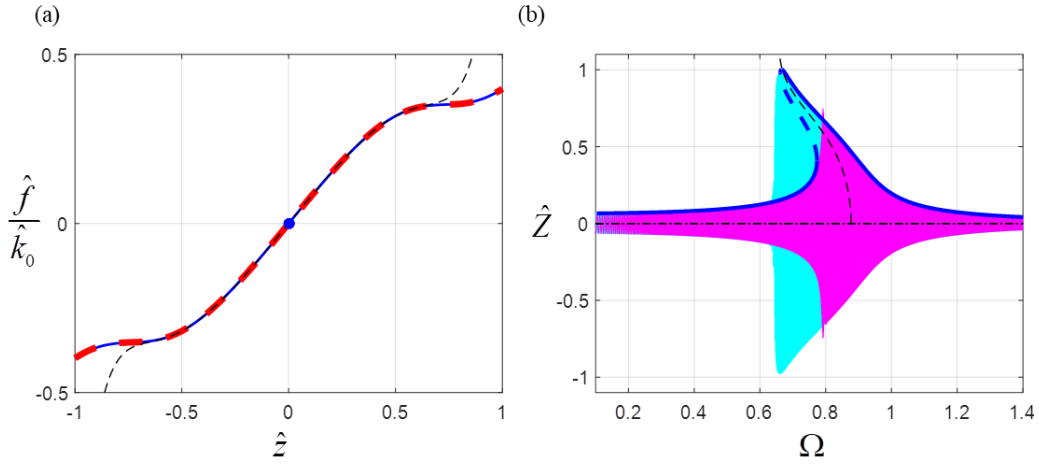


Figure 20. System response for $\theta = 1.9$. (a) Normalized force-displacement curve of exact (thick solid line), actual polynomial (thick dashed line) and Taylor polynomial (thin dashed line) solution. Small circles denote static equilibrium configurations. (b) Frequency response curve with stable (thick solid lines) and unstable (thick dashed lines) branches, backbone curve (thin dashed line), static equilibrium configuration (thin dash-dotted line, sweep-down (thin lighter/cyan line), and sweep-up (thin darker/magenta line).

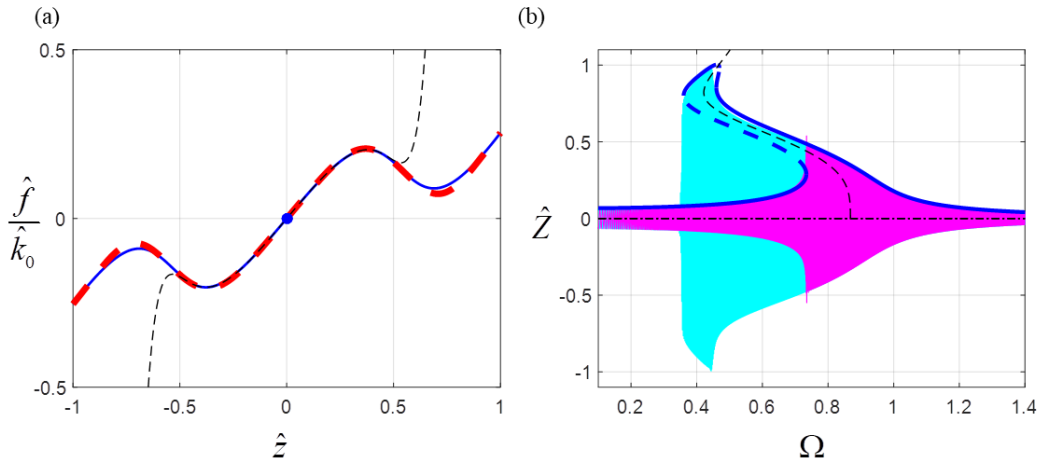


Figure 21. System response for $\theta = 3.0$. (a) Normalized force-displacement curve of exact (thick solid line), actual polynomial (thick dashed line) and Taylor polynomial (thin dashed line) solution. Small circles denote static equilibrium configurations. (b) Frequency response curve with stable (thick solid lines) and unstable (thick dashed lines) branches, backbone curve (thin dashed line), static equilibrium configuration (thin dash-dotted line, sweep-down (thin lighter/cyan line), and sweep-up (thin darker/magenta line).

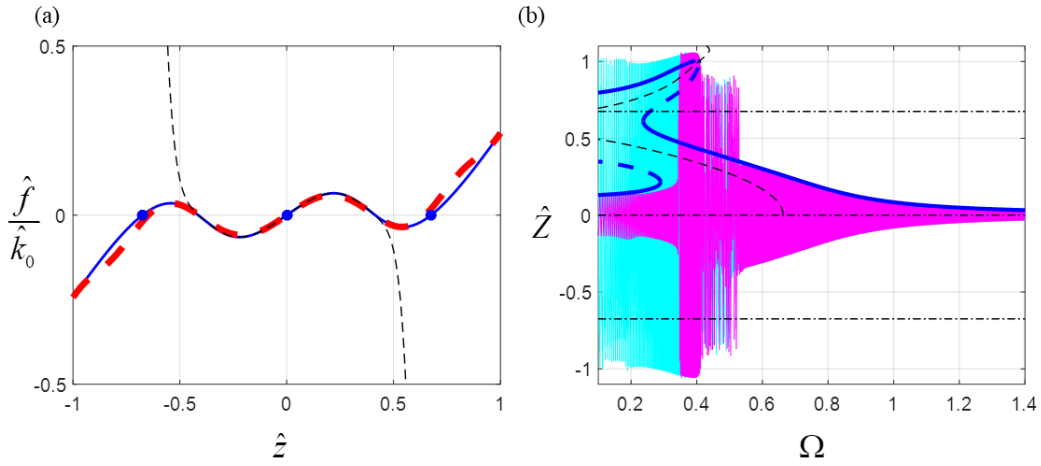


Figure 22. System response for $\theta = 3.6$. (a) Normalized force-displacement curve of exact (thick solid line), actual polynomial (thick dashed line) and Taylor polynomial (thin dashed line) solution. Small circles denote static equilibrium configurations. (b) Frequency response curve with stable (thick solid lines) and unstable (thick dashed lines) branches, backbone curve (thin dashed line), static equilibrium configuration (thin dash-dotted line, sweep-down (thin lighter/cyan line), and sweep-up (thin darker/magenta line).

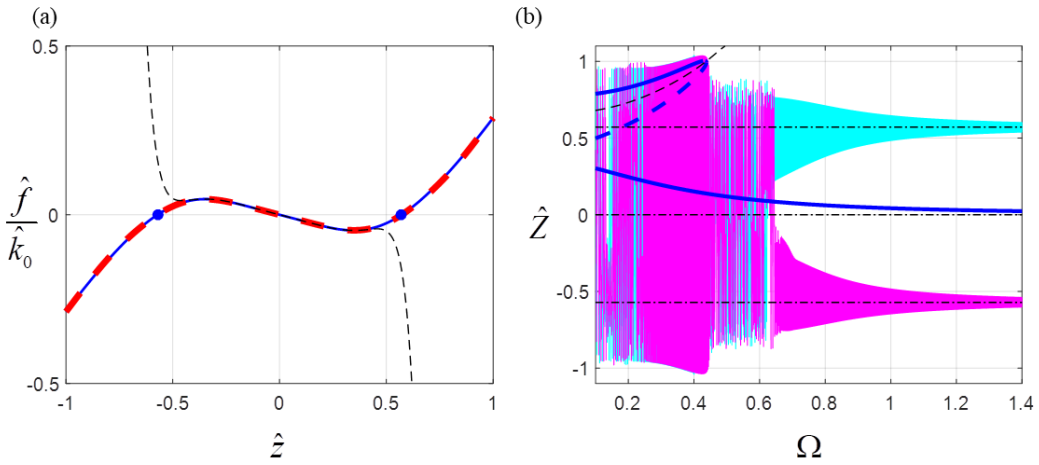


Figure 23. System response for $\theta = 4.6$. (a) Normalized force-displacement curve of exact (thick solid line), actual polynomial (thick dashed line) and Taylor polynomial (thin dashed line) solution. Small circles denote static equilibrium configurations. (b) Frequency response curve with stable (thick solid lines) and unstable (thick dashed lines) branches, backbone curve (thin dashed line), static equilibrium configuration (thin dash-dotted line, sweep-down (thin lighter/cyan line), and sweep-up (thin darker/magenta line).

5 CONCLUSIONS

In this study, a mechanical device able to realise different nonlinear force-displacement characteristics is conceptualised and analysed. The device is simple and compact, and its geometry can be adapted on purpose to achieve qualitatively different stiffness behaviours. Examples are provided as quasi-zero stiffness for small deflections, hardening and softening nonlinearity, softening-hardening behaviour, quasi-zero stiffness for large deflections, bi-stable and tri-stable characteristics. A theoretical investigation has been performed which revealed the fundamental issues and the design strategy. Analytical expressions for static and dynamic performance are analysed and validated by numerical simulations. The device enables engineers to exploit the most convenient characteristic and even adaptively change it over time to accomplish different needs. Potential applications are foreseen for vibration energy harvesting, vibration isolation, nonlinear energy sink, shock isolation, snap-through systems, robotic soft-grippers, and elastic potential energy storage and release.

Funding: This research did not receive any specific grant from funding agencies in the public, commercial, or not-for-profit sectors**.**

Conflict of Interest: The author declares that he has no conflict of interest

APPENDIX A. Supplementary data

A supplementary animation provided for this article can be found online.

APPENDIX B. Polynomial coefficients

The force, its first and second derivative reported in Eq.(2), Eq.(3) and Eq.(4), respectively, are evaluated at full-span, $\hat{z}=1$, and half-span, $\hat{z}=1/2$, to give

$$g_1 = \hat{f}\Big|_{\hat{z}=1} = 1 + 2\left((1-a)\left(1 - \frac{1}{\sqrt{(-1+a)^2 + b^2}} \right) + (1+a)\left(1 - \frac{1}{\sqrt{(1+a)^2 + b^2}} \right) \right) k$$

$$g_2 = \frac{\partial \hat{f}}{\partial \hat{z}}\bigg|_{\hat{z}=1} = 1 + \left(4 + b^2 \left(-\frac{2}{\left((-1+a)^2 + b^2\right)^{3/2}} - \frac{2}{\left((1+a)^2 + b^2\right)^{3/2}} \right) \right) k$$

$$g_3 = \frac{\partial^2 \hat{f}}{\partial \hat{z}^2}\bigg|_{\hat{z}=1} = 6b^2 \left(\begin{array}{l} \dfrac{1}{\left((-1+a)^2 + b^2\right)^{5/2}} + \dfrac{1}{\left((1+a)^2 + b^2\right)^{5/2}} + \\ a\left(-\dfrac{1}{\left((-1+a)^2 + b^2\right)^{5/2}} + \dfrac{1}{\left((1+a)^2 + b^2\right)^{5/2}} \right) \end{array} \right) k$$

$$g_4 = \hat{f}\Big|_{\hat{z}=\frac{1}{2}} = \frac{1}{2} + 2\left(\left(\frac{1}{2} - a \right)\left(1 - \frac{1}{\sqrt{\left(-\frac{1}{2} + a \right)^2 + b^2}} \right) + \left(\frac{1}{2} + a \right)\left(1 - \frac{1}{\sqrt{\frac{1}{4} + a + a^2 + b^2}} \right) \right) k$$

$$g_5 = \frac{\partial \hat{f}}{\partial \hat{z}}\bigg|_{\hat{z}=\frac{1}{2}} = 1 + \left(4 + b^2 \left(-\frac{2}{\left(\left(-\frac{1}{2} + a \right)^2 + b^2 \right)^{3/2}} - \frac{2}{\left(\frac{1}{4} + a + a^2 + b^2 \right)^{3/2}} \right) \right) k$$

$$g_6 = \frac{\partial^2 \hat{f}}{\partial \hat{z}^2}\bigg|_{\hat{z}=\frac{1}{2}} = 6b^2 \left(\begin{array}{l} a\left(-\dfrac{1}{\left(\left(-\frac{1}{2} + a \right)^2 + b^2 \right)^{5/2}} + \dfrac{1}{\left(\frac{1}{4} + a + a^2 + b^2 \right)^{5/2}} \right) + \\ \dfrac{1}{2}\left(\dfrac{1}{\left(\left(-\frac{1}{2} + a \right)^2 + b^2 \right)^{5/2}} + \dfrac{1}{\left(\frac{1}{4} + a + a^2 + b^2 \right)^{5/2}} \right) \end{array} \right) k$$

The polynomial expression in Eq. (14) is then used with the first condition given by Eq. (6), i.e. $k_1 = \hat{k}_1$, and the following linear system of six equations is obtained

$$\begin{bmatrix} 1 & 1 & 1 & 1 & 1 & 1 \\ 3 & 5 & 7 & 9 & 11 & 13 \\ 6 & 20 & 42 & 72 & 110 & 156 \\ \frac{1}{2^3} & \frac{1}{2^5} & \frac{1}{2^7} & \frac{1}{2^9} & \frac{1}{2^{11}} & \frac{1}{2^{13}} \\ \frac{3}{2^2} & \frac{5}{2^4} & \frac{7}{2^6} & \frac{9}{2^8} & \frac{11}{2^{10}} & \frac{13}{2^{12}} \\ \frac{6}{2} & \frac{20}{2^3} & \frac{42}{2^5} & \frac{72}{2^7} & \frac{110}{2^9} & \frac{156}{2^{11}} \end{bmatrix} \cdot \begin{Bmatrix} k_3 \\ k_5 \\ k_7 \\ k_9 \\ k_{11} \\ k_{13} \end{Bmatrix} = \begin{Bmatrix} g_1 \\ g_2 \\ g_3 \\ g_4 \\ g_5 \\ g_6 \end{Bmatrix} - \begin{Bmatrix} \hat{k}_1 \\ \hat{k}_1 \\ 0 \\ \hat{k}_1/2 \\ \hat{k}_1 \\ 0 \end{Bmatrix}$$

which is solved for the six unknown coefficients, the to give

$$k_3 = \frac{1}{648}\left(-9720\hat{k}_1 - 601g_1 + 81g_2 - 3g_3 + 31232g_4 - 5376g_5 + 384g_6\right)$$

$$k_5 = \frac{1}{324}\left(28188\hat{k}_1 + 4117g_1 - 561g_2 + 21g_3 - 110336g_4 + 23424g_5 - 2112g_6\right)$$

$$k_7 = \frac{1}{648}\left(-158760\hat{k}_1 - 41557g_1 + 5757g_2 - 219g_3 + 679424g_4 - 145152g_5 + 16512g_6\right)$$

$$k_9 = \frac{1}{162}\left(56376\hat{k}_1 + 23215g_1 - 3303g_2 + 129g_3 - 256640g_4 + 52032g_5 - 7008g_6\right)$$

$$k_{11} = -\frac{2}{81}\left(9720\hat{k}_1 + 5423g_1 - 807g_2 + 33g_3 - 46336g_4 + 8832g_5 - 1344g_6\right)$$

$$k_{13} = \frac{8}{81}\left(648\hat{k}_1 + 445g_1 - 69g_2 + 3g_3 - 3200g_4 + 576g_5 - 96g_6\right)$$

APPENDIX C. Taylor series coefficients

Expanding Eq. (2) in Taylor series for small deflections up to the 13-th order results in

$$\hat{f} \approx t_1\hat{z} + t_3\hat{z}^3 + t_5\hat{z}^5 + t_7\hat{z}^7 + t_9\hat{z}^9 + t_{11}\hat{z}^{11} + t_{13}\hat{z}^{13}$$

where the series coefficients are reported below

$$t_1 = 1 + \left(4 - \frac{4\hat{b}^2}{\left(\hat{a}^2 + b^2\right)^{3/2}} \right) \hat{k}$$

$$t_3 = \frac{2\hat{b}^2 \left(-4\hat{a}^2 + \hat{b}^2\right) \hat{k}}{\left(\hat{a}^2 + \hat{b}^2\right)^{7/2}}$$

$$t_5 = -\frac{3\hat{b}^2 \left(8\hat{a}^4 - 12\hat{a}^2\hat{b}^2 + \hat{b}^4\right) \hat{k}}{2\left(\hat{a}^2 + \hat{b}^2\right)^{11/2}}$$

$$t_7 = \frac{\hat{b}^2 \left(-64\hat{a}^6 + 240\hat{a}^4\hat{b}^2 - 120\hat{a}^2\hat{b}^4 + 5\hat{b}^6\right) \hat{k}}{4\left(\hat{a}^2 + \hat{b}^2\right)^{15/2}}$$

$$t_9 = -\frac{5\hat{b}^2 \left(128\hat{a}^8 - 896\hat{a}^6\hat{b}^2 + 1120\hat{a}^4\hat{b}^4 - 280\hat{a}^2\hat{b}^6 + 7\hat{b}^8\right) \hat{k}}{32\left(\hat{a}^2 + \hat{b}^2\right)^{19/2}}$$

$$t_{11} = \frac{3\hat{b}^2 \left(-512\hat{a}^{10} + 5760\hat{a}^8\hat{b}^2 - 13440\hat{a}^6\hat{b}^4 + 8400\hat{a}^4\hat{b}^6 - 1260\hat{a}^2\hat{b}^8 + 21\hat{b}^{10}\right) \hat{k}}{64\left(\hat{a}^2 + \hat{b}^2\right)^{23/2}}$$

$$t_{13} = -\frac{7\hat{b}^2 \left(1024\hat{a}^{12} - 16896\hat{a}^{10}\hat{b}^2 + 63360\hat{a}^8\hat{b}^4 - 73920\hat{a}^6\hat{b}^6 + 27720\hat{a}^4\hat{b}^8 - 2772\hat{a}^2\hat{b}^{10} + 33\hat{b}^{12}\right) \hat{k}}{256\left(\hat{a}^2 + \hat{b}^2\right)^{27/2}}$$

REFERENCES

[1] G. Gatti, M.J. Brennan, B. Tang, Some diverse examples of exploiting the beneficial effects of geometric stiffness nonlinearity. Mechanical Systems and Signal Processing. 125 (2019) 4-20. https://doi.org/10.1016/j.ymssp.2018.08.024.

[2] A.M. Giri, S.F. Ali, A. Arockiarajan, Dynamics of symmetric and asymmetric potential well-based piezoelectric harvesters: A comprehensive review. Journal of Intelligent Material Systems and Structures 32 (2021) 1881-1947. https://doi.org/10.1177/1045389X20978292

[3] T. Yang, S. Zhou, S. Fang, W. Qin, D.J. Inman, Nonlinear vibration energy harvesting and vibration suppression technologies: Designs, analysis, and applications. Applied Physics Reviews 8 (2021) 031317. https://doi.org/10.1063/5.0051432

[4] R.A. Ibrahim, Recent advances in nonlinear passive vibration isolators, Journal of Sound and Vibration 314 (2008) 371-452.

[5] Z. Lu, Z. Wang, Y. Zhou, X. Lu, Nonlinear dissipative devices in structural vibration control: A review. Journal of Sound and Vibration 423 (2018) 18-49. https://doi.org/10.1016/j.jsv.2018.02.052

[6] A.F. Vakakis, Passive nonlinear targeted energy transfer. Philosophical Transactions of the Royal Society A: Mathematical, Physical and Engineering Sciences 376 (2018) 20170132. http://dx.doi.org/10.1098/rsta.2017.0132

[7] H. Ding, L.-Q. Chen, Designs, analysis, and applications of nonlinear energy sinks. Nonlinear Dynamics 100 (2020) 3061-3107. https://doi.org/10.1007/s11071-020-05724-1

[8] D. F. Ledezma-Ramírez, P. E. Tapia-González, N. Ferguson, M.J. Brennan, B. Tang, Recent advances in shock isolation: An overview and future possibilities. Applied Mechanics Reviews 71 (2019) 060802. https://doi.org/10.1115/1.4044190

[9] T. Heidlauf, T. Klotz, C. Rode, T. Siebert, O. Rohrle, A continuum-mechanical skeletal muscle model including actin-titin interaction predicts stable contractions on the descending limb of the force-length relation. PLoS Comput Biol 13 (2017) e1005773. http://dx.doi.org/10.1371/journal.pcbi.1005773.

[10] D.L. Morgan, U. Proske, D. Warren, Measurements of muscle stiffness and the mechanism of elastic storage of energy in hopping kangaroos. Journal of Physiology 282 (1978) 253-61. http://dx.doi.org/10.1113/jphysiol.1978.sp012461.

[11] A. Struzik, J. Zawadzki, Estimation of potential elastic energy during the countermovement phase of a vertical jump based on the force–displacement curve. Acta of Bioengineering and Biomechanics 21 (2019) 153-60. http://dx.doi.org/10.5277/ABB-01316-2019-01.

[12] A.K. Lappin, J.A. Monroy, J.Q. Pilarski, E.D. Zepnewski, D.J. Pierotti, K.C. Nishikawa, Storage and recovery of elastic potential energy powers ballistic prey capture in toads. Journal of Experimental Biology 209 (2006) 2535-53. http://dx.doi.org/10.1242/jeb.02276.

[13] G. Yan, H.-X. Zou, S. Wang, L.-C. Zhao, Z.-Y. Wu, W.-M. Zhang, Bio-inspired vibration isolation: Methodology and design. Applied Mechanics Reviews 73 (2021) 020801. http://dx.doi.org/10.1115/1.4049946

[14] G. Yan, H.-X. Zou, S. Wang, L.-C. Zhao, Z.-Y. Wu, W.-M. Zhang, Bio-inspired toe-like structure for low-frequency vibration isolation. Mechanical Systems and Signal Processing 162 (2022) 108010. https://doi.org/10.1016/j.ymssp.2021.108010

[15] H. Dai, X. Jing, Y. Wang, X. Yue, J. Yuan, Post-capture vibration suppression of spacecraft via a bio-inspired isolation system. Mechanical Systems and Signal Processing 105 (2018) 214-240. https://doi.org/10.1016/j.ymssp.2017.12.015

[16] Y. Zhang, Q. Cao, The recent advances for an archetypal smooth and discontinuous oscillator. International Journal of Mechanical Sciences 214 (2022) 106904. https://doi.org/10.1016/j.ijmecsci.2021.106904

[17] Q. Cao, M. Wiercigroch, E.E. Pavlovskaia, C. Grebogi, J.M.T. Thompson, Archetypal oscillator for smooth and discontinuous dynamics. Physical Review E 74 (2006) 046218. http://dx.doi.org/10.1103/PhysRevE.74.046218

[18] Y. Han, Q. Cao, Y. Chen, M. Wiercigroch, A novel smooth and discontinuous oscillator with strong irrational nonlinearities. Science China Physics, Mechanics & Astronomy 55 (2012) 1832–1843. http://dx.doi.org/10.1007/s11433-012-4880-9

[19] Q. Cao, A. Léger, A Smooth and Discontinuous Oscillator: Theory, Methodology and Applications. Springer 2016.

[20] T. Yang, Q. Cao, Dynamics and performance evaluation of a novel tristable hybrid energy harvester for ultra-low level vibration resources. International Journal of Mechanical Sciences 156 (2019) 123-136. https://doi.org/10.1016/j.ijmecsci.2019.03.034

[21] F. Zhao, J.C. Ji, K. Ye, Q. Luo, Increase of quasi-zero stiffness region using two pairs of oblique springs. Mechanical Systems and Signal Processing 144 (2020) 106975. https://doi.org/10.1016/j.ymssp.2020.106975

[22] G. Gatti, Effect of Parameters on the Design of a Suspension System with Four Oblique Springs. Shock and Vibration (2021) 5556088. https://doi.org/10.1155/2021/5556088

[23] Z. Hao, Q. Cao, M. Wiercigroch, Nonlinear dynamics of the quasi-zero-stiffness SD oscillator based upon the local and global bifurcation analyses. Nonlinear Dynamics 87 (2017) 987–1014. https://doi.org/10.1007/s11071-016-3093-6

[24] R. Tian, Q. Cao, S. Yang, The codimension-two bifurcation for the recent proposed SD oscillator. Nonlinear Dynamics 59 (2010) 19–27. https://doi.org/10.1007/s11071-009-9517-9

[25] C.Liu, X. Jing, Vibration energy harvesting with a nonlinear structure. Nonlinear Dynamics 84 (2016) 2079-2098. https://doi.org/10.1007/s11071-016-2630-7

[26] T.D. Le, K.K. Ahn, Experimental investigation of a vibration isolation system using negative stiffness structure. International Journal of Mechanical Sciences 70 (2013) 99-112. https://dx.doi.org/10.1016/j.ijmecsci.2013.02.009

[27] J. Bian, X. Jing, Analysis and design of a novel and compact X-structured vibration isolation mount (X-Mount) with wider quasi-zero stiffness range. Nonlinear Dynamics, 101 (2020) 2195-2222. https://doi.org/10.1007/s11071-020-05878-y

[28] X. Jing, Y. Chai, X. Chao, J. Bian, In-situ adjustable nonlinear passive stiffness using X-shaped mechanisms. Mechanical Systems and Signal Processing 170 (2022) 108267. https://doi.org/10.1016/j.ymssp.2021.108267

[29] G. Donga, X. Zhanga, S. Xiea, B. Yan, Y. Luo, Simulated and experimental studies on a high-static-low-dynamic stiffness isolator using magnetic negative stiffness spring. Mechanical Systems and Signal Processing 86 (2017) 188-203. http://dx.doi.org/10.1016/j.ymssp.2016.09.040

[30] S. Lo Feudo, C. Touzé, Boisson, G. Cumunel, Nonlinear magnetic vibration absorber for passive control of a multi–storey structure. Journal of Sound and Vibration 438 (2019) 33-53. https://doi.org/10.1016/j.jsv.2018.09.007

[31] X. Liu, X. Huang, H. Hua, On the characteristics of a quasi-zero stiffness isolator using Euler buckled beam as negative stiffness corrector. Journal of Sound and Vibration 332 (2013) 3359-3376. https://dx.doi.org/10.1016/j.jsv.2012.10.037

[32] C. Liu, R. Zhao, K. Yu, H.P. Lee, B. Liao, A quasi-zero-stiffness device capable of vibration isolation and energy harvesting using piezoelectric buckled beams. Energy 233 (2021) 121146. https://doi.org/10.1016/j.energy.2021.121146

[33] M.-Q. Niu, L.-Q. Chen, Nonlinear vibration isolation via a compliant mechanism and wire ropes. Nonlinear Dynamics, in press https://doi.org/10.1007/s11071-021-06588-9

[34] Y. Tian, C. Zhou, F. Wang, K. Lu, Y. Yuan, M. Yang, D. Zhang, Design of a flexure-based mechanism possessing low stiffness and constant force. Review of Scientific Instruments 90 (2019) 105005. https://doi.org/10.1063/1.5119276

[35] K. Wang, J. Zhou, Y. Chang, H. Ouyang, D. Xu, Y. Yang. A nonlinear ultra-low-frequency vibration isolator with dual quasi-zero-stiffness mechanism. Nonlinear Dynamics 101 (2020) 755–773. https://doi.org/10.1007/s11071-020-05806-0

[36] Z. Hao, Q. Cao, The isolation characteristics of an archetypal dynamical model with stable-quasi-zero-stiffness. Journal of Sound and Vibration 340 (2015) 61–79. http://dx.doi.org/10.1016/j.jsv.2014.11.038

[37] A.D. Shaw, G. Gatti, P.J.P. Gonçalves, B. Tang, M.J. Brennan, Design and test of an adjustable quasi-zero stiffness device and its use to suspend masses on a multi-modal structure. Mechanical Systems and Signal Processing 152 (2021) 107354. https://doi.org/10.1016/j.ymssp.2020.107354

[38] G. Gatti, A.D. Shaw, P.J.P. Gonçalves, M.J. Brennan, On the detailed design of a quasi-zero stiffness device to assist in the realisation of a translational Lanchester damper. Mechanical Systems and Signal Processing 164 (2022) 108258. https://doi.org/10.1016/j.ymssp.2021.108258

[39] D.D. Quinn, A.L. Triplett, L.A. Bergman, A.F. Vakakis, Comparing Linear and Essentially Nonlinear Vibration-Based Energy Harvesting. Journal of Vibration and Acoustic 133 (2011) 011001. https://doi.org/10.1115/1.4002782.

[40] G. Gatti, Fundamental insight on the performance of a nonlinear tuned mass damper. Meccanica 53 (2018) 111–123. https://doi.org/10.1007/s11012-017-0723-0.

[41] T. Detroux, G. Habib, L. Masset, G. Kerschen, Performance, robustness and sensitivity analysis of the nonlinear tuned vibration absorber. Mechanical Systems and Signal Processing 60-61 (2015) 799-809. http://dx.doi.org/10.1016/j.ymssp.2015.01.035.

[42] M.J. Brennan, G. Gatti, The characteristics of a nonlinear vibration neutralizer. Journal of Sound and Vibration 331 (2012) 3158-3171. http://dx.doi.org/10.1016/j.jsv.2012.02.010

[43] P.S. Low, R. Ramlan, H.A. Ghani, N.S. Muhammad, Experimental Analysis on the Transduction Coefficient of a Non-Linear Electromagnetic Energy Harvesting Device with Softening Stiffness. International Journal of Automotive and Mechanical Engineering 17 (2020) 7816-7831. https://doi.org/10.15282/ijame.17.2.2020.01.0582.

[44] G. Yan, H.-X. Zou, S. Wang, L.-C. Zhao, Q.-H. Gao, T. Tan, W.-M. Zhang, Large stroke quasi-zero stiffness vibration isolator using three-link mechanism. Journal of Sound and Vibration 478 (2020) 115344. https://doi.org/10.1016/j.jsv.2020.115344

[45] G. Gatti, Optimizing elastic potential energy via geometric nonlinear stiffness, Communications in Nonlinear Science and Numerical Simulation 103 (2021) 106035. https://doi.org/10.1016/j.cnsns.2021.106035

[46] Y. Liu, Y. Zhang, Q. Xu, Design and Control of a Novel Compliant Constant-Force Gripper Based on Buckled Fixed-Guided Beams. IEEE/ASME Transactions on mechatronics, 22 (2017) 476-486. https://doi.org/10.1109/TMECH.2016.2614966.

[47] Q.J. Cao, Y.W. Han, T.W. Liang, M. Wiercigroch, S. Piskarev, Multiple Buckling and Codimension-Three Bifurcation Phenomena of a Nonlinear Oscillator. International Journal of Bifurcation and Chaos 24 (2014) 1430005. http://dx.doi.org/10.1142/S0218127414300055

[48] R.L. Harne, K.W. Wang, A review of the recent research on vibration energy harvesting via bi-stable systems. Smart Materials and Structures 22 (2013) 023001. https://doi.org/10.1088/0964-1726/22/2/023001

[49] B. Tang, X. Meng, F.L. Zhang, M.J. Brennan, G.K. Lau, Z. Wang, L.Y. Feng, Theoretical and practical investigation into the use of a bio-inspired ‘‘click” mechanism for the flight motor of a micro air vehicle. International Journal of Micro Air Vehicles 9 (2017) 136-145. https://doi.org/10.1177/1756829317695562.

[50] B. Yan, N. Yu, H. Ma, C. Wu, A theory for bistable vibration isolators. Mechanical Systems and Signal Processing 167 (2022) 108507. https://doi.org/10.1016/j.ymssp.2021.108507.

[51] H.-T. Li, H. Ding, X.-J. Jing, W.-Y. Qin, L.-Q. Chen. Improving the performance of a tri-stable energy harvester with a staircase-shaped potential well. Mechanical Systems and Signal Processing 159 (2021) 107805. https://doi.org/10.1016/j.ymssp.2021.107805

[52] V.G. Cleante, M.J. Brennan, G. Gatti, D.J. Thompson, Energy harvesting from the vibrations of a passing train: Effect of speed variability. Journal of Physics: Conference Series 744 (2016), 012080. https://doi.org/10.1088/1742-6596/744/1/012080

[53] M.J. Brennan, G. Gatti, Harvesting Energy From Time-Limited Harmonic Vibrations: Mechanical Considerations. Journal of Vibration and Acoustics, 139 (2017) 051019. https://doi.org/10.1115/1.4036867

[54] S. Li, W. Gao, D. Yurchenko, X. Wang, J. Wang, X. Liu, Novel spacer-tuned-mass-damper system for controlling vibrations of hangers. Mechanical Systems and Signal Processing 167 (2022) 10853. https://doi.org/10.1016/j.ymssp.2021.108537

[55] D. Zou, G. Liu, Z. Rao, T. Tan, W. Zhang, W.-H. Liao, A device capable of customizing nonlinear forces for vibration energy harvesting, vibration isolation, and nonlinear energy sink. Mechanical Systems and Signal Processing 147 (2021) 107101. https://doi.org/10.1016/j.ymssp.2020.107101